Nanoscale

COMMUNICATION

View Article Online
View Journal | View Issue

Cite this: *Nanoscale*, 2026, **18**, 3537

Received 13th October 2025,
Accepted 9th December 2025

DOI: 10.1039/d5nr04311e

rsc.li/nanoscale

Surface engineering of titanium dioxide nanotube electrodes *via in situ* carbon incorporation for enhanced supercapacitance

Soumya Jha and R. Prasanth *

Titanium dioxide (TiO_2) is an attractive electrode material for supercapacitors due to its high surface area, good chemical stability, and relatively low cost, although its poor conductivity remains the major limiting factor. This can limit the rate at which charges can be stored and released in the electrode, affecting the overall performance of the supercapacitors. Herein, we have incorporated carbon in one of the practical ways to explore the potential of TiO_2 as the capacitance of supercapacitors is directly related to the surface area. The electrochemically fabricated titanium dioxide nanotubes infused with carbon have an enhanced surface area and improved performance due to their exceptional ability to store charge and conduct electricity like a metal. At the nanoscale, incorporating carbon dopants into a crystal lattice of titanium dioxide by ultrathin coating on the surface improves its characteristics significantly. The meticulous control of dopant concentration within the TiO_2 lattice enables precise adjustment of the carrier density. A comprehensive characterization study using XRD, HRSEM, HRTEM, Raman, and XPS techniques was employed to elucidate the influence of carbon dopants on the TiO_2 lattice structure. Contact angle measurement was recorded to understand the wettability of the electrode material in different systems. At a current density of 0.1 mA cm^{-2}, the electrode examined in 1 M HCl had a stunning areal capacitance of 21.125 mF cm^{-2}. Following electrochemical characterization, surface studies have been conducted to understand the comprehensive view of the electrode's functionality and structural availability. The investigation reveals the promising application of carbon-coated samples as high-performance electrode materials for supercapacitors.

1. Introduction

The growing visibility of local and global environmental concerns has fuelled an increased demand for clean, renewable energy sources.[1–3] Various efforts have been implemented to tackle the challenge of generating and consuming renewable energy and developing a sustainable society.[4,5] To accomplish these demands, electrochemical energy conversion and storage technologies have been identified as ideal replacements for traditional non-renewable sources due to their environmental friendliness, cost-effectiveness, portability, and versatility.[6,7] These innovations have been the source of the fast development that has spurred a recent wave of flexible, wearable, and portable electronic gadget innovation because of their many benefits, including being small, light weight, and flexible. These energy storage devices make energy management efficient. Flexible energy storage devices, in particular, have gained a lot of attention due to the various electrical systems they may use.[8] Supercapacitors have been steadily taking over the market thanks to their extended cycle life, high power output, and quick charge and discharge features. Supercapacitors (SCs) are regarded as one of the most promising power sources because of their high-power density, long life cycle, fast charge–discharge rates, and straightforward mechanisms for portable systems and diverse automotive applications.[9–13]

Owing to the restricted amount of space readily accessible, areal capacitance is a significant factor in the engineering of supercapacitors as sources of power for electronic devices. Carbon materials, such as carbon nanotubes (CNTs), activated carbon, and graphene, are desirable for supercapacitors because they have a high specific surface area, high electrical conductivity, and excellent stability.[2,14–17] Carbon-based supercapacitor electrodes are employed in flexible electronics due to their high rigidity and power density.[18–20] One issue with carbon materials as electrode materials is that they have limited ionic reachability and poor energy density. On the other hand, supercapacitors made of transition metal oxides, such as RuO_2, MnO_2, NiO, TiO_2, and Fe_2O_3, have elevated specific capacitance and energy densities.[17,21–23] Although RuO_2-based electrode materials show high specific capacitance among all transition metal-based oxides, they are not cost-effective.[5] Consequently, alternative transition materials, such as TiO_2, have been employed as promising materials for applying supercapacitors.[21,24] TiO_2 nanotubes are among the most intriguing structures for energy storage

Madanjeet School of Green Energy Technology, Pondicherry Central University, Pondicherry, India. E-mail: prasanth.get@pondiuni.edu.in

because they are readily available, inexpensive to fabricate, and have stable chemical properties. Their one-dimensional structure has the advantages of unidirectional electron transport, high surface area, and interconnectivity, all of which are required for supercapacitor electrode materials.[25–27] They are utilized as supercapacitor electrodes, yet it has been noted that the inherent stiffness of metal oxides results in low power density and poor flexibility in supercapacitors.

To overcome these shortcomings, an array of techniques, including hydrogenation, preferred crystal axis orientation, annealing, plasma treatment, and electrochemical treatment, have been used to increase the capacitance of the nanotube electrodes.[23,26,28–30] TiO_2 nanotube arrays (TNTs) with oxygen vacancies created by a one-step reduction method in $NaBH_4$ have been shown to have an exceptional supercapacitance performance.[31] Doping is one such method, and doping non-metallic materials with transition metal-based supercapacitors could increase their capacitance as the energy storage mechanism is due to an increase in the exchange of charges between the electrode and the electrolyte through a fast-faradaic redox reaction.[13,21,32–34] Tamgadge *et al.* have reported that fluorine doping of anatase TiO_2 using a hydrothermal technique has increased its electrochemical performance.[35] Liu *et al.* have successfully fabricated Sn doped TiO_2 nanotube arrays with Ti vacancies to showcase a conceptually different fabrication technique, although the areal specific capacitance attained needs room for improvement.[36] Kumar *et al.* have reported a study that presents an *in situ* carbon supported-TiO_2 electrode made from sucrose and TiO_2 powder, with an efficient specific capacitance of 277.72 F g^{-1} for charge storage and 180 F g^{-1} in an aqueous electrolyte.[37]

While numerous efforts have been made to enhance the specific capacitance of TiO_2-based nanomaterial electrodes, the incorporation of carbon into TNTs presents a considerable challenge.[37,38] The inherent low electronic conductivity of these materials results in a significant decline in capacitance at elevated scan rates. This underscores the need for further investigation into the critical role of carrier density in nanotube electrodes. Therefore, combining metal oxides with carbon materials makes sense to create composites that can improve and lessen both components' drawbacks. Our present strategy focuses on streamlining the fabrication process by doping prepared samples with carbon through anodization and the following annealing step. The only carbon source that produced a skinny layer of carbon on the TNTs' surface was ethylene glycol. The annealing phase was carried out in environments devoid of oxygen (argon) to determine its impact doping in the resultant nanotube electrode. We have boosted the electrochemical capacitance and improved the defect concentration by refining the fabrication method.

2. Experimental details

2.1 Sample preparation

By the electrochemical anodization technique and subsequent carbonization, C–TiO_2 nanotube arrays were created. 1-D nanotube arrays were fabricated using a two-electrode electrochemical system where Ti foil (Sigma-Aldrich, 99.7% trace metal basis, 2 mm thickness) was the working electrode. In comparison, the Pt (2.5 cm × 2.5 cm) mesh (Sigma-Aldrich, 99.9% trace metal basis, 52 gauze) served as the counter electrode. This titanium foil (10 cm × 10 cm) was cut into small pieces of 2 cm × 1 cm and then was polished with silicon carbide grade sheets of progressively finer abrasive grit size ranging from 60 to 2000, and then they were ultrasonically cleaned for 10 minutes in water, ethanol and acetone to remove residual particles before anodization. A Keithley 2400 Source Meter unit was used to apply a consistent potential of 40 V between the two electrodes during electrochemical anodization for 3 hours. Ammonium fluoride (Sigma-Aldrich, ≥99.7% purity), ethylene glycol (Sigma-Aldrich, Reagent plus, ≥99.7% purity), and water were the components of the electrolyte solution; the water content was maintained at 4 vol%, while the concentration of ammonium fluoride was kept at 0.4 wt%. To coat carbon, the as-prepared TiO_2 nanotubes were dipped in ethylene glycol for varying durations, ranging from one hour to twelve hours, and the excess solution was drained. These immersed samples underwent a three-hour vacuum drying process at 90 °C, followed by an additional 500 °C argon annealing to attain the crystallinity of the sample. These prepared samples were labelled as BT, C1, C3 and C12, where BT refers to bare TiO_2 nanotubes, and C1, C3, and C12 denote the carbon-coated TNT samples obtained after 1, 3, and 12 hours of immersing, respectively.

2.2 Morphological characterization

The high-resolution scanning electron microscope (HRSEM), Thermo Scientific Apreo S, was utilized to analyze the morphology such as diameter, wall thickness, porosity, and length of the nanotubes. ImageJ and machine learning techniques were used for all measurements and the analysis that followed. To understand the porous nature and uniformity of the deposited layers and to further analyze the lattice fringes and crystalline nature of the prepared samples, High-Resolution Transmission Electron Microscopy (HRTEM) analysis was carried out using a Thermo Scientific Talos F200S G2 instrument. Using Cu Kα radiation at (λ = 1.5406 Å), X-ray diffraction (XRD; Bruker USA D8 Advance, Davinci) was used to record the diffraction patterns. The phase of the nanotubes was detected and measured using Raman spectroscopy (micro-RAMAN; LabRAM HR, Horiba) using an internal 50 mW Ar ion laser source with a wavelength of 785 nm. X-ray photoelectron spectroscopy (XPS; Thermo Fisher Scientific, Model K-Alpha) was used to investigate the surface chemical composition of the TNT thin film and carbon coated TiO_2 nanotube (C/TNT) thin film.

2.3 Electrochemical characterization

An electrode setup was used for the electrochemical studies. Ag/AgCl served as the reference electrode, platinum mesh served as the counter electrode, and TNT and C/TNT electrodes were employed as the working electrodes. As the electrolyte, a

1 M HCl (Sigma-Aldrich, Emplura, ≥99.7% purity) aqueous solution was used. In the voltage range of −0.6 V to +0.2 V, cyclic voltammetry measurements were performed at various scan speeds ranging from 5 mV to 100 mV. Galvanostatic charge–discharge was conducted at multiple discharge rates ranging from 0.1 mA cm^{-2} to 1 mA cm^{-2}. The Mott–Schottky plots, produced by measuring the impedance at a fixed frequency of 1 kHz at various potentials concerning the reference electrode, were used to compute the carrier density. In EIS, a perturbation signal with an amplitude of 10 mV (peak-to-peak voltage) was utilized, with a frequency range of 0.1 Hz to 100 kHz and Nova software was used to fit the resulting data.

3. Results and discussion

3.1 Morphological and structural characterization

Titanium foil was oxidized in an electrolyte system with fluoride to create titania nanotubular arrays (TNTs), and self-organized nanotube layers formed through chemical dissolution, field-assisted oxidation, and field-assisted dissolution. The synthesized nanotube arrays were dipped using a carbon precursor solution to produce carbon coatings. The high-resolution scanning electron microscopy (HRSEM) pictures of the samples BT, C1, C3 and C12 that were anodized in 4 vol% water in ethylene glycol containing ammonium fluoride (0.4 wt%) electrolyte for a total of 3 hours and dipped in ethylene glycol for 1, 3, 6, and 12 hours are depicted in Fig. 1(a–d). The carbon doping did not affect the morphology and structure of the TiO_2 nanotube arrays. Each of these five electrode materials has a tube length of around 25 ± 0.5 μm. The wall thicknesses of nanotubes BT, C1, C3, and C12 are 16 ± 10 nm, 19 ± 10 nm, 21 ± 10 nm, and 26 ± 10 nm, respectively (as shown in Fig. S1(b)), and their average diameters are 104 ± 10 nm, 95 ± 10 nm, 81 ± 10 nm, 79 ± 10 nm, and 69 ± 10 nm. The average titanium nanotube diameter shows a decreasing tendency, while the apparent wall thickness exhibits a relative increase with higher carbon content, which is consistent with the presence of carbon coating on the TNT walls as also indicated by Raman mapping.

Using image processing techniques in conjunction with these HRSEM images, the porosity of the samples was further interpreted, along with the pore size distribution of TNTs.[39,40] Filtration theories have been utilized to account for the deposition likelihood of solid particles, and the structure of both C-coated and porous TNTs is modelled using the bundle of curved tubes technique illustrated in Fig. 1(e–h). The use of SEM images quantitatively to quantify and identify the size of the TNT spaces using the watershed segmentation technique is an innovative aspect of this study. Based on the discussed method for image processing, the calculated porosity and pore size distribution of BT, C1, C3, and C12 are in range of 0.22–0.28 as discussed in Table S1 with marginal error. These errors suggest that carbon coating and doping insinuate only marginal changes in porosity. By comparing the porosity results, it is observed that porosity is enhanced by coating and doping of carbon. Furthermore, with pore space segmentation mapping, it is observed that uniform pores have been forming, and spaces, where pores are not seen, depict the presence of carbon coating.

TEM was used to corroborate the tubular shape of the carbon doped sample, which is a hollow tube-like structure with a rough surface morphology, as shown in Fig. 2. The HRTEM image of BT as shown in Fig. 2(a & b) shows smooth, uniform tube walls with well-defined lattice fringes, as previously observed in the HRSEM data. In contrast, the carbon-doped TiO_2 exhibits comparatively thicker and roughened tube walls due to the conformal carbon layer deposited when immersed in EG. This modification not only alters the surface texture but also subtly influences the local contrast in HRTEM images, distinguishing the doped sample from the bare nanotubes. According to Fig. 2(c), the tube diameter of C12 was around 56 nm, with the wall thickness around 26 nm, which is consistent with the HRSEM analysis. Selected Area Electron Diffraction (SAED) and HRTEM investigation of the sample's morphology and crystallinity revealed a greater resolution of 0.35 nm interlayer distance, which correlates to the (0 1 1) planes of anatase TiO_2 (ICSD pattern: 98-010-6862). The previously mentioned data also subtly support the *d*-spacing of TiO_2 seen in XRD, which is covered in more detail in the later section.

The phase and crystallite size of the anodization-prepared nanotubes and carbon-coated TNTs were ascertained by X-ray diffraction analysis illustrated in Fig. 3. The samples of pure titania nanotubes and carbon-coated titania nanotube show a crystalline anatase phase that is primarily orientated in the (0 1 1) direction. Peaks at 25.42°, 48.24°, 52.22°, 62.47°, 63.12°, 76.39° and 82.63°, respectively, correlate to the planes of the anatase phase in TiO_2 nanotube arrays (0 1 1), (0 2 0), (0 2 2), (1 2 3), (0 2 4), (0 3 1), and (0 3 3).[41] The average crystallite size for BT, C1, C3, and C12 was calculated using the W–H plot analysis as shown in Fig. S2, which is 39.27 nm, 36.39 nm, 32.42 nm and 15.42 nm, respectively. This confirmed that the introduction of doping usually creates lattice distortion, which increased lattice strain hence confirms that peak broadening attributed to lattice strain.

The samples as prepared exhibited distinctive TiO_2 anatase peaks that aligned well with the standard ICSD patterns 98-010-6862 (anatase) and 98-007-1963 (Ti). XRD clarified the anatase-phase crystal structures of the BT, C1, C3 and C12 samples. A decrease in crystallite size indicated that coating in carbon visibly reduces the crystallinity of the sample.

Using Raman spectroscopy, additional structural investigation of bare TiO_2 nanotubes and carbon-coated TiO_2 nanotubes was conducted, and the outcomes are shown in Fig. 4. There were four distinct peaks of TiO_2 observed in each spectrum, which represents E_g at 145 cm^{-1}, B_{1g} at 395 cm^{-1}, A_{1g} at 516 cm^{-1} and E_{1g} at 636 cm^{-1} of the anatase TiO_2 Raman spectra in the samples BT, C1, C3 and C12. The symmetric stretching vibration of the O–Ti–O bond in TiO_2 was the primary source of the peak correlating with the B_{1g} mode, while the O–Ti–O antisymmetric bending vibration caused the

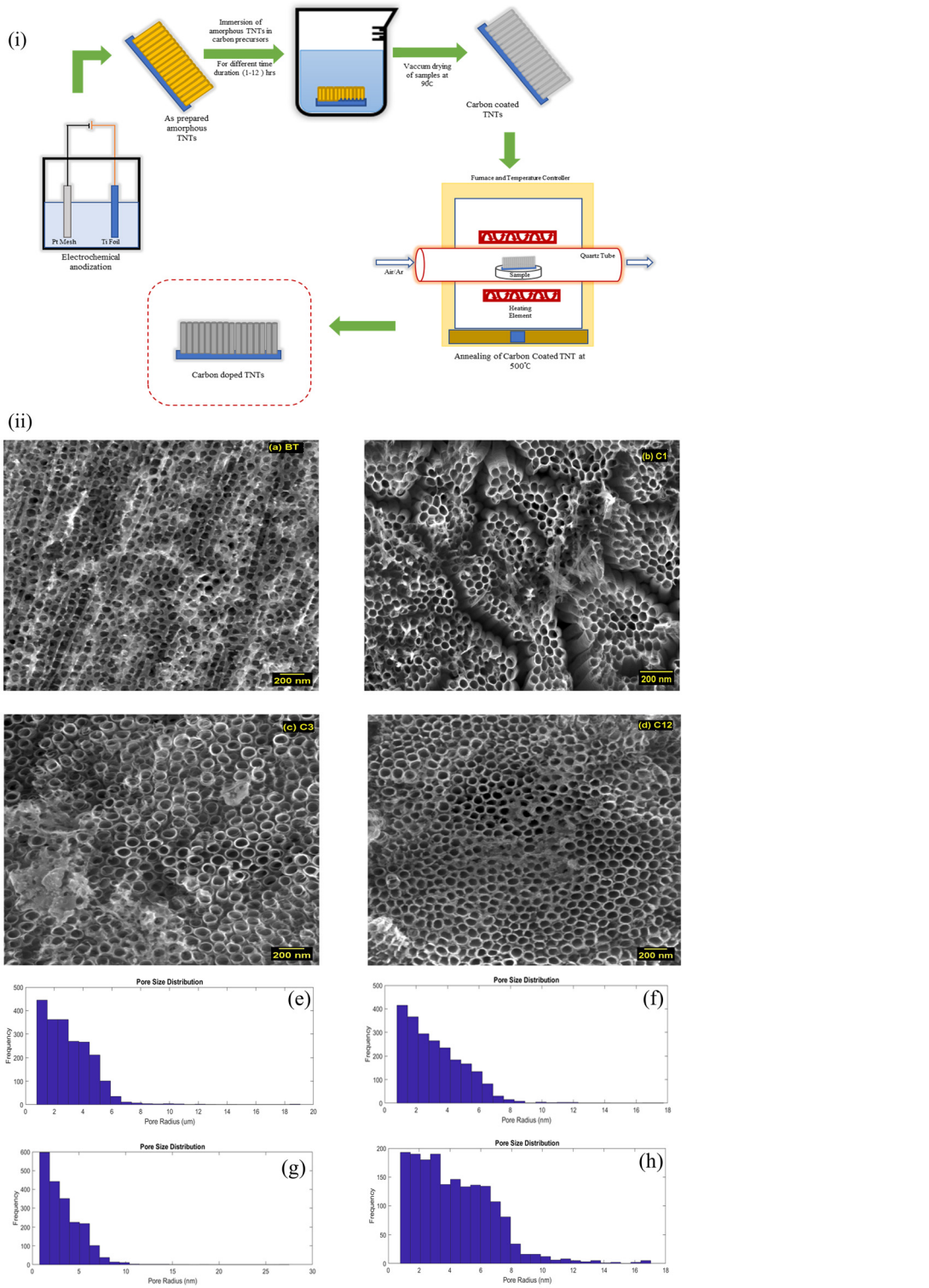

Fig. 1 (i) Schematic representation of the different stages of the sample preparation of the carbon-doped TNTs. (ii) HRSEM and pore size distribution images of the (a and e) BT, (b and f) C1, (c and h) C3, (d and g) C6 and (e and h) C12 samples.

A_{1g} peak. In C12, additional peaks were visible, corresponding to the D band at 1334.75 cm^{-1} and the G band corresponding to 1596.61 cm^{-1}, which apparently conveys the presence of carbon in the TNT.[20] One peak, the D band, was observed at 1334 cm^{-1} and indicated the disorders (defects, vacancies, bond disruption, *etc.*) produced in the carbon lattice. The G band, or second peak, was seen at 1596 cm^{-1}, a widely used indication of graphitic structures. The vibrational modes of

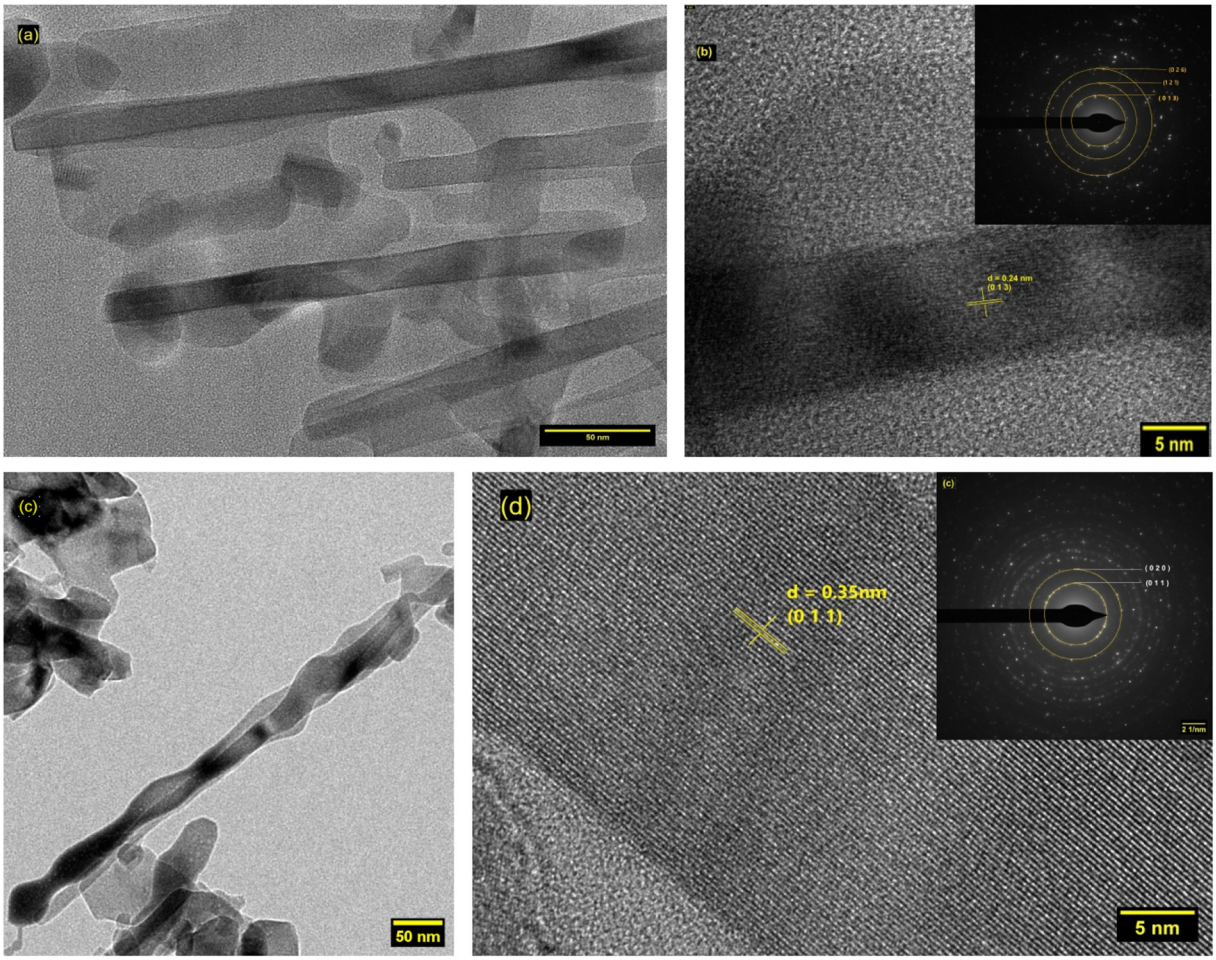

Fig. 2 (a) TEM of BT; (b) HRTEM image of BT (the inset shows the SAED pattern of BT with the lattice plane); (c) TEM of C12; and (d) the HRTEM image of C12 (the inset shows the SAED pattern of C12 with the lattice plane).

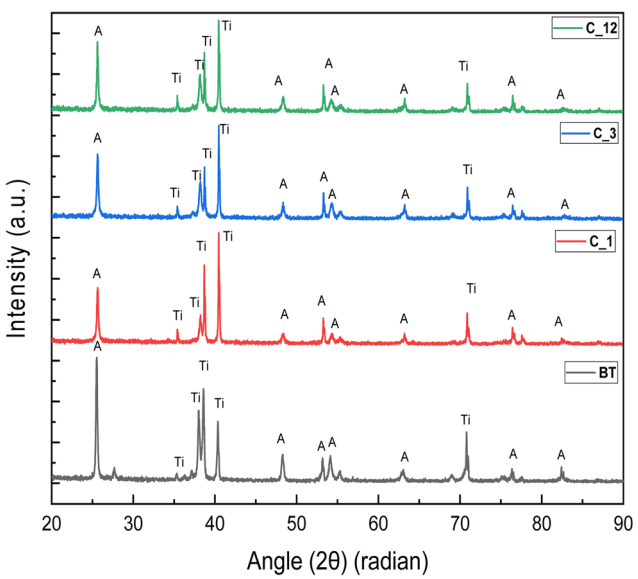

Fig. 3 X-ray diffraction patterns of BT, C1, C3 and C12.

the sp^2-bonded carbon atoms produce this band. The degree of disorder in the carbonaceous materials is represented by the D and G peaks' intensity ratio (I_D/I_G). For the carbon-coated TiO_2 material as developed, the I_D/I_G ratio is 0.84, indicating a moderate level of long-range graphitization layer order in the graphitic structures. Additionally, a simultaneous red shift in the A_{1g} and B_{1g} peaks of the C12 sample is noted, with the A_{1g} peak shifting from 516 cm^{-1} to 506 cm^{-1} and the B_{1g} peak shifting from 395 cm^{-1} to 382 cm^{-1}. The observed red-shift can be attributed to lattice expansion, which reduces the phonon frequency. Improved crystallinity minimizes defect-induced stresses and enhances lattice order, thereby supporting this shift. This suggests that the sample can retain its crystalline structure even after graphitization.

The uniformity of the carbon coating on TNT was assessed through Raman peak intensity mapping of all samples. Raman mapping is a method that provides comprehensive details about the chemical and structural composition of a material by combining spatial imaging and Raman spectroscopy. By moving a laser beam over a sample and collecting Raman spectra at each spot, it is possible to create maps that show the

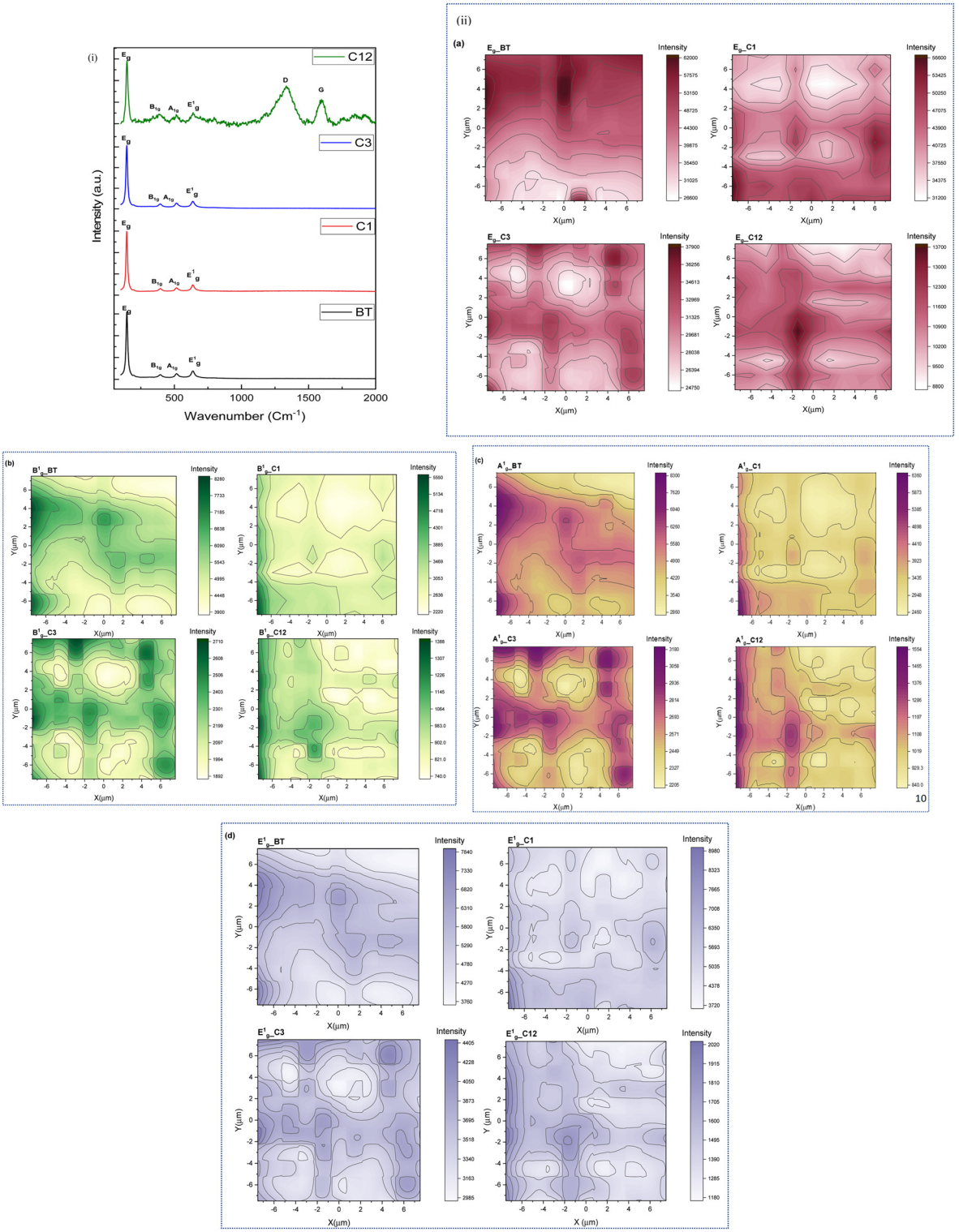

Fig. 4 (i) Raman spectra of BT, C1, C3 and C12. (ii) Raman mapping of the Stokes line for (a) $E_g(\nu_1)$, (b) $B_{1g}(\nu_2)$, (c) $A_{1g}(\nu_4)$ and (d) $E_{1g}(\nu_6)$ of different BT, C1, C3 and C12.

distribution of structural or chemical components.[42] As shown in Fig. 4(ii), the Raman signals have been detected from 121 (11 × 11) spots 11 in the square arrays of points. There is 2 μm separating the horizontal and vertical locations and the modes $E_g(\nu_1)$ (~145 cm^{-1}), $B_{1g}(\nu_2)$ (~395 cm^{-1}), $A_{1g}(\nu_4)$ (~516 cm^{-1}), and $E_{1g}(\nu_6)$ (~517.5 cm^{-1}) are associated with these peaks. It was observed that Stokes line intensity of peaks was decreasing in all modes when deposition time was increased, which indi-

cated that the coating of carbon onto TiO_2 nanotubes can obscure the characteristic Stokes lines. Furthermore, it was observed that the coating of carbon was lighter in C1 than in C3 and C12. The uniform and consistent Raman intensity across the mapped region suggests that carbon incorporation does not create local inhomogeneities in the TiO_2 lattice, which indirectly supports the conclusion of a uniform distribution of carbon. This consistency shows that the carbon was doped uniformly and under control throughout the whole surface of the TNT.

3.2 Surface characterization and elemental composition

Measurements using X-ray photoelectron spectroscopy (XPS), as illustrated in Fig. 5 and S3, were required to comprehend the relationship between the carbon dopant and the TiO_2 nanotube arrays. The survey spectrum illustrated in Fig. 5(a) allows for observing the binding energies of the electrons of the elements O, Ti, and C. As shown in the high-resolution XPS spectra of Ti 2p in Fig. 5(b), the distinctive peaks at 459.2 eV and 464.8 eV correspond to Ti $2p^{3/2}$ and Ti $2p^{1/2}$, respectively. For the pure TNT, *i.e.*, BT, and C-doped TNT, *i.e.*, C12, the splitting energies between Ti $2p^{1/2}$ and Ti $2p^{3/2}$ are around 5.8 eV, indicating that Ti in TNTAs primarily resides in the form of Ti^{4+}. It was found that the binding energy of Ti $2p^{1/2}$ in C12 (465.1 eV) was positively shifted compared to BT's (464.8 eV). Furthermore, the binding energy of Ti $2p^{3/2}$ in C12 was increased by roughly 0.20 eV. The significant interaction between Ti^{4+} and C components can be due to the positive shift in binding energies. After deconvolution, as shown in Fig. 5(d), two peaks of O 1s at 530.39 eV and 531.1 eV were seen, corresponding to bulk oxygen binding (Ti–O) and the surface hydroxyl group and lattice oxygen of TiO_2, respectively. The lattice sites of oxygen atoms were occupied by carbon atoms, as shown by these results. Furthermore, the O 1s of C12 nanotube arrays exhibited a sizeable positive shift in the binding energy from BT nanotube arrays, as shown in Fig. 5(e). The C 1s spectra of C12 were fitted to three peaks at 284.78, 286.38, and 288.95 eV, indicating that three different chemical forms of carbon existed in the samples, as shown in Fig. 5(f). The presence of C in the sample as Ti–O–C was indicated by the signal at 288.95 eV.

3.3 Contact angle measurement

Wettability of electrode materials greatly influences the charge storage efficiency, ion diffusion and penetration of the electrolyte, which is one of the important aspects of supercapacitive performance. After doping of TiO_2, the contact angle slightly increased from 7.79° ± 1° to 14.51° ± 1°, indicating a slight decrease in hydrophilicity. However, the electrode surface retained strong compatibility with the electrolyte, facilitating efficient high ion diffusion and charge accumulation. Fig. 6(a) shows the advancing contact angles of BT, C1, C3, and C12 samples in distilled water. As shown in Fig. 6(b), 1 M HCl, which also functioned as the electrolyte in the further electrochemical study, was also used to determine the contact angles. Contact angle was slightly increased when measured with 1 M HCl compared to water, suggesting a marginal difference in surface wettability depending on the probing liquid. This variation can be attributed to the ionic nature and surface tension differences between water and the acidic electrolyte. Despite the increase, the surface remained sufficiently hydrophilic to ensure good electrode–electrolyte interaction, which is critical for promoting efficient ion transport and enhancing charge storage performance in supercapacitor applications.

3.3 Electrochemical characterization

3.3.1 Cyclic voltammetry. Capacitive performance of BT, C1, C3, and C12 was measured using cyclic voltammetry (CV). Fig. 8(a) illustrates the potential window of −0.6 V to +0.2 V in which CV measurements of BT, C1, C3, and C12 were performed in 1 M HCl. The electrodes exhibited the supercapacitive behavior of TiO_2 nanotube arrays by yielding quasi rectangular-shaped CV curves (Fig. 7(a)). Additionally, a linear rise in current density was observed with an increase in scan rate from 10 mV s^{-1} to 100 mV s^{-1}, with no alteration in the form of the acquired curve. This was consistent with the non-faradaic behaviour.

Areal capacitance was directly proportional to the integrated area under the CV curve. It depends on the scan rate, the total area of the sample, and the potential window in which it operates.[10,26,37] Fig. 7(a) shows the cyclic voltammetric curves of the carbon-doped and bare TiO_2 samples. The areal capacitance of the samples BT, C1, C3 and C12 was 2.5 mF cm^{-2}, 5.31 mF cm^{-2}, 11.47 mF cm^{-2} and 21.125 mF cm^{-2}, respectively. It was observed that C12 shows higher capacitance compared to the other samples. Furthermore, the computed areal capacitance values for different scan rates ranging 10 mV s^{-1}, 20 mV s^{-1}, 30 mV s^{-1}, 40 mV s^{-1}, 50 mV s^{-1} and 100 mV s^{-1} of C12 are as follows 21.125 mF cm^{-2}, 18.6 mF cm^{-2}, 17.25 mF cm^{-2}, 15.9 mF cm^{-2}, 11.7 mF cm^{-2} and 8.3 mF cm^{-2}, respectively. Retention of shape as observed in CV at higher scan rates indicates good rate capability, while a decrease in areal capacitance was observed, which indicated that the ion access was reduced to deeper pores when the scan rates were increased. Higher scan rates allowed ions to participate on the double layer of the electrode's surface. Lower scan rates increased the capacitance because ions from the electrolyte can interact with the bulk and access practically all the pores of the electrode material, which resulted in an elevated capacitance value for the same electrode material.

3.3.2 Charge discharge analysis. In addition, a galvanostatic charge–discharge (GCD) analysis was performed to evaluate the performance of the carbon-doped nanotube sample. All GCD measurements were performed over the potential range of −0.6 V to 0.2 V at varied current densities of 0.1, 0.2, and 0.3 mA cm^{-2} (Fig. 8(a–d)). All GCD curves showed symmetrical voltage variations across steady areal scan rates over time. This illustrates the outstanding capacitive performance with high reversibility during the charging and discharging cycles. In short, the material can store and release energy effectively with low losses. An areal capacitance of 18.79, 12.28 and 8.07 mF cm^{-2} was obtained at different rates of 0.1, 0.2, and

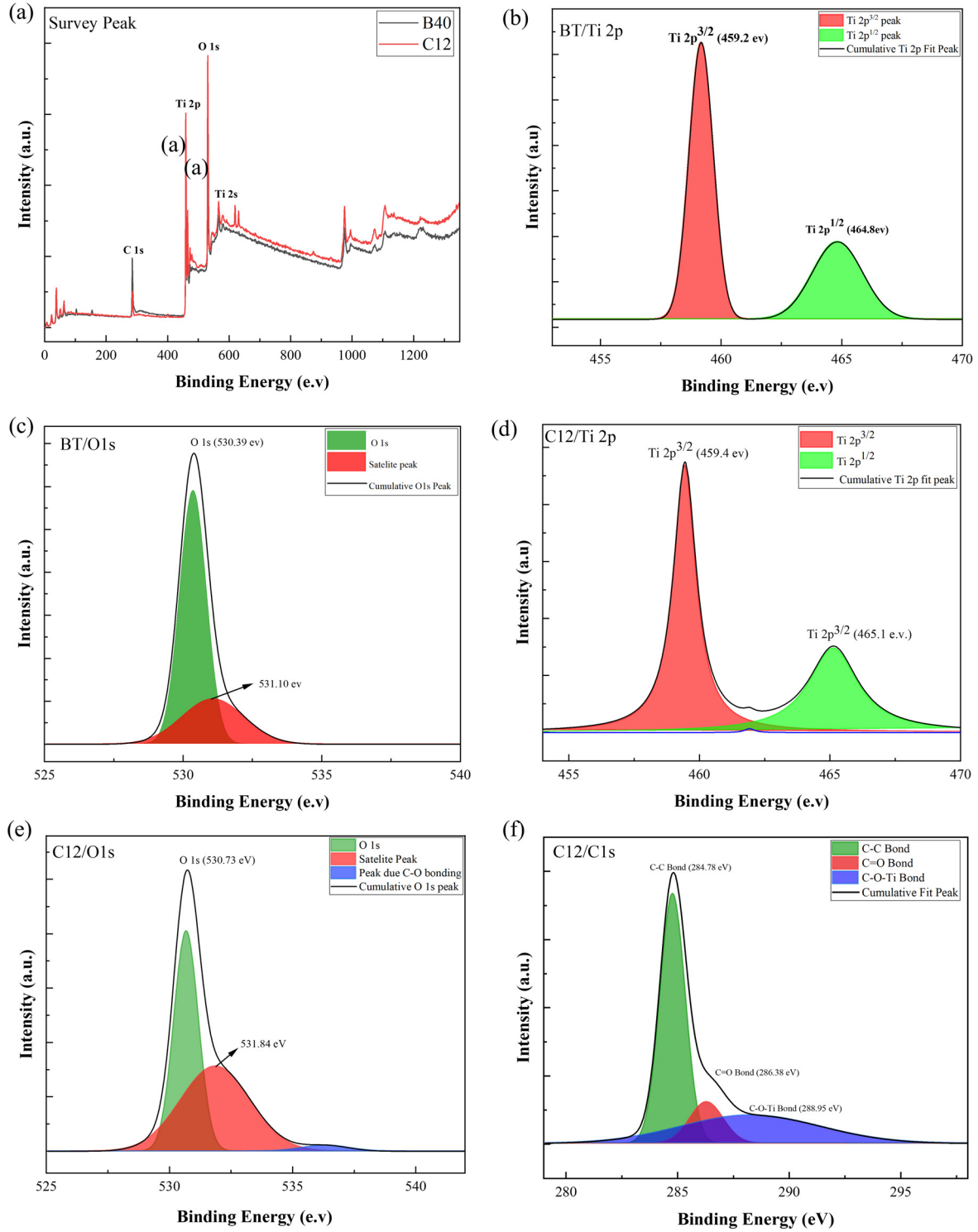

Fig. 5 (a) XPS survey peak of BT and C12 samples. (b) Ti 2p peak of BT. (c) Ti 2p peak of C12. (d) O 1s peak of BT. (e) O 1s peak of C12. (f) C 1s peak of C12.

0.3 mA cm^{-2} of the C12 sample. Similarly, 3.69, 8.46 and 12.46 mF cm^{-2} areal capacitance was observed for BT, C1, and C3, respectively, at 0.1 mA cm^{-2}. The carbon-doped sample dipped for 12 h resulted in higher capacitance values for the nanotube samples than those annealed in oxygen. The study showed that the areal capacitance fluctuates with the discharge rate in doped carbon samples. A low discharge rate of 0.1 mA cm^{-2} resulted in an areal capacitance of 14.48 mF

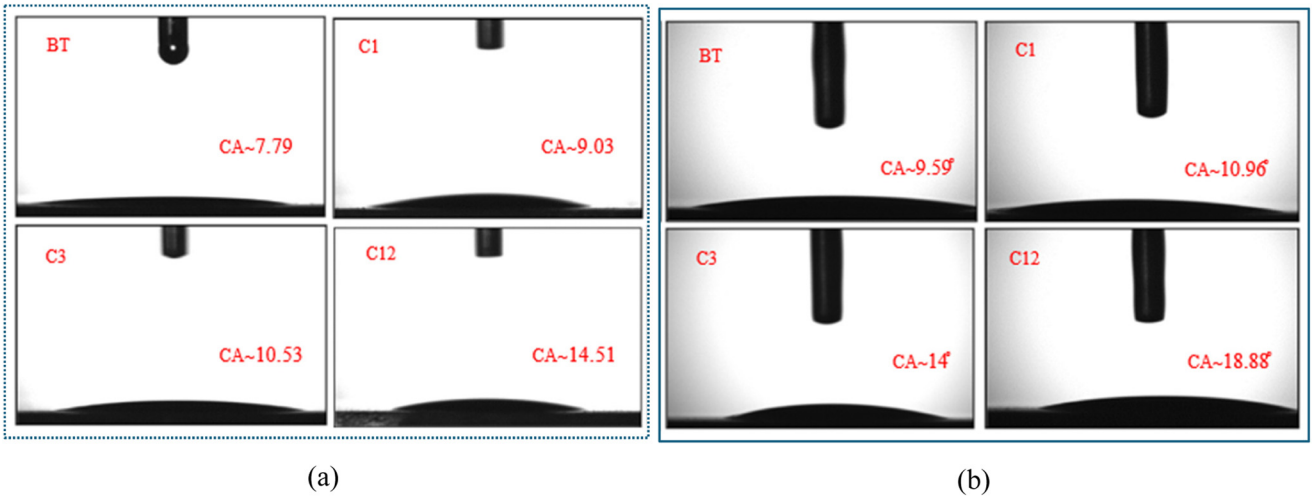

Fig. 6 Advancing contact angle measurement of BT, C1, C3 and C12 using (a) water and (b) 1 M HCl.

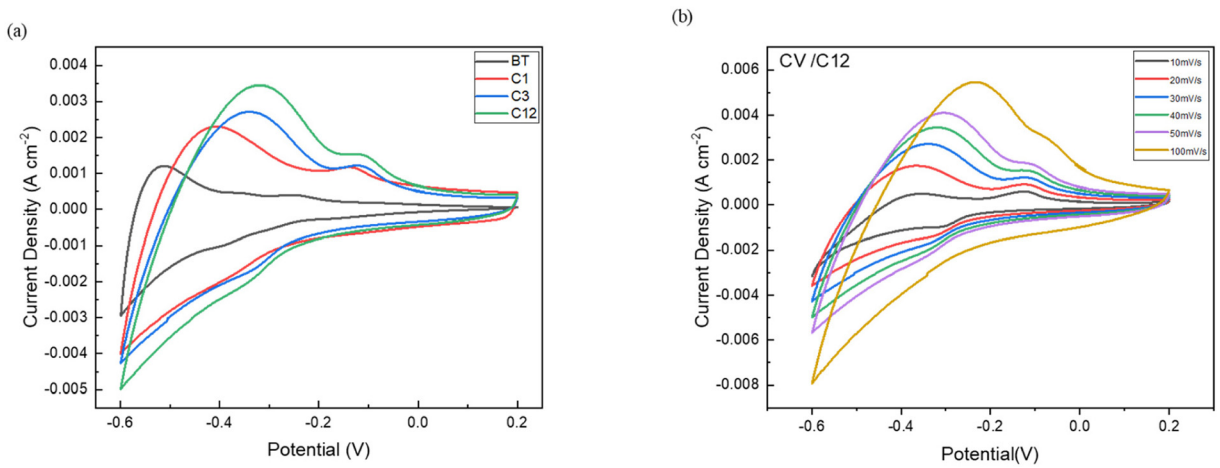

Fig. 7 (a) CV curves of BT, C1, C3 and C12 recorded at 30 mV s^{-1}. (b) CV curves of the C12 sample recorded at different scan rates starting from 10 mV s^{-1} to 100 mV s^{-1}.

cm^{-2}, and when discharged at 1 mA cm^{-2}, the value reduces to 9.56 mF cm^{-2}. Fig. 8(e) presumably showcases this trend of various doped carbon samples. The electrochemical stability of supercapacitors was critical for their practicality and economic viability. The cycle stability of the nanotube electrodes was evaluated over 10 000 times, and 74% capacitance retention was reported. The electrodes showed good stability even after 10 000 cycles. Table 1 presents a compilation of performance data for different TiO_2-doped electrodes, as reported in the existing literature.[26,43–45] The enhanced electrical conductivity and surface area of the carbon-doped electrode were responsible for this better performance. Because of the carbon-doped electrode's greater surface area and electrical conductivity, performance was improved.

Following a long-term cycling stability test, XRD of BT, C1, C3 and C12, FESEM and XPS analyses of the C12 sample were also assessed. Even if the XRD peaks were attenuated or faded, peaks belonging to anatase TiO_2 were observed, and the peak patterns had not altered further after the long-term stability test, according to the XRD peaks, as shown in Fig. 9(a). The nanotube structure was well preserved following the stability test, according to the FESEM image in Fig. 9(b). However, the carbon layer that was formed on top of TiO_2 peeled off as a result of the prolonged galvanostatic charge–discharging cycle in 1 M HCl. This stability was further confirmed by the XPS data, which are displayed in Fig. 9(c), which further confirmed the components' consistent binding energies. It was established that the steady binding energies of Ti, O, and C components, indicating sustained stability. This strong bond between TiO_2 and carbon dopants ensures the material's durability and reliability for extended periods. Furthermore, comparisons

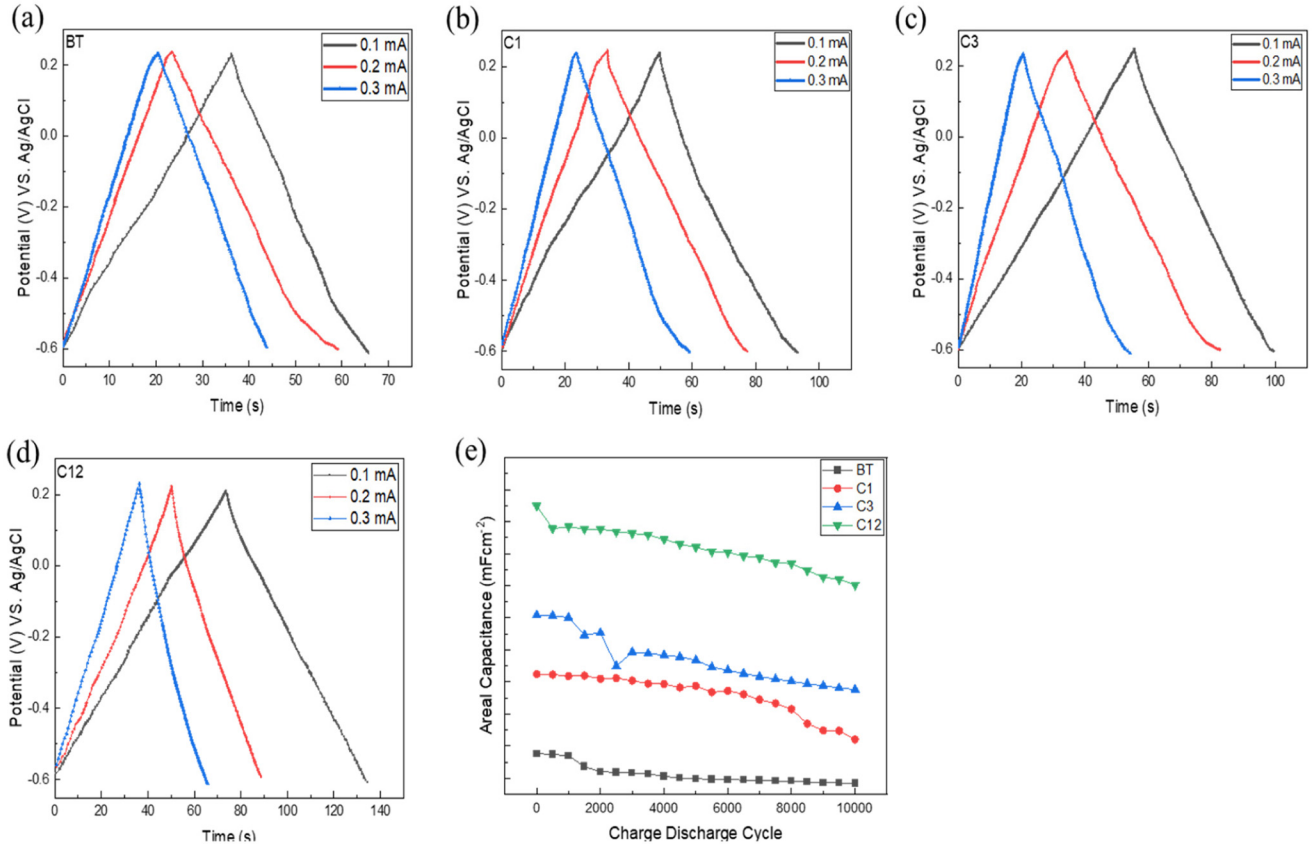

Fig. 8 (a–d) Galvanostatic charge discharge curve of BT, C1, C3 and C12 at different scan rates of 0.1, 0.2 and 0.3 mA cm^{-2} and (e) galvanostatic cycling data of the different samples calculated at 1 mA cm^{-2}.

Table 1 Comparison of electrochemical performance of the TiO_2-based materials

Materials	Electrolyte	Potential window (V)	C_s (mF cm^{-2})	Cycle life	Ref.
TiO_2 nanotubes	1 M HCl	0.0 to 0.5	1.78 mF cm^{-2}@5 mV s^{-1}	76% after 5000 cycles@500 mV s^{-1}	43
Hydrogenated TiO_2 nanotubes	0.5 M Na_2SO_4	0 to 0.8	3.24 mF cm^{-2}@100 mV s^{-1}	97% after 10 000 cycles@100 mV s^{-1}	49
Hydrogenated TiO_2	0.5 M Na_2SO_4	−0.2 to 0.6	1.05 mF cm^{-2}@100 mV s^{-1}	93.8% after 1000 cycles@0.1 mA cm^{-2}	29
N-TiO_2	1 M Na_2SO_4	0 to 1	2.48 mF cm^{-2}@10 mV s^{-1}	88.7% after 1000 cycles@200 mV s^{-1}	50
Black TiO_2	1 M Na_2SO_4	0 to 0.8	15.6 mF cm^{-2}@100 mV s^{-1}	96% after 5000 cycles@100 mV s^{-1}	44
Oxygen vacant TiO_2 nanotubes	1 M HCl	0.0 to 0.5	20.09 mF cm^{-2}@0.1 mA cm^{-2}	90% after 5000 cycles@500 mV s^{-1}	26
Carbon coated TiO_2 nanotubes	1 M HCl	−0.6 to 0.2	21.125 mF cm^{-2}@10 mV s^{-1}	81% after 3000 cycles@0.1 mA cm^{-2}	Current work

of the CV, GCD and EIS curves of the C12 before and after using are displayed in Fig. S4 in the SI. All performance metrics confirm reduction in the cycling stability of C12 and the simultaneous reduction in CV area and GCD discharge time signals a substantial loss of stored charge. This degradation was further validated by the Nyquist plot (EIS), which showed significant kinetic limitations due to an increase in internal resistance (R_s) and, most prominently, the charge transfer resistance (R_{ct}), directly observed through the enlargement of the high-frequency semicircle.

3.3.3 Electrochemical impedance and the Mott–Schottky analysis. Electrochemical impedance spectroscopy (EIS) was used to analyze the electrochemical behavior of the electrode further in order to evaluate its performance. The EIS's measuring frequency was measured between 10 kHz and 0.1 Hz. Fig. 10(a) depicts Nyquist plots ($-Z''$ against Z') for the samples BT, C1, C3, and C12. The Nyquist plot ($-Z''$ *vs.* Z') of the samples begins with a depressed semicircle in the high-intermediate region and ends with a straight line in the low-frequency region. The diameter of the semicircle provides a rough estimation of the electrode's charge transfer resistance. The near-vertical line exhibits the pseudocapacitive characteristic of the electrode material.[46–48,51] The equivalent circuit consists of the following components: the intrinsic resistance

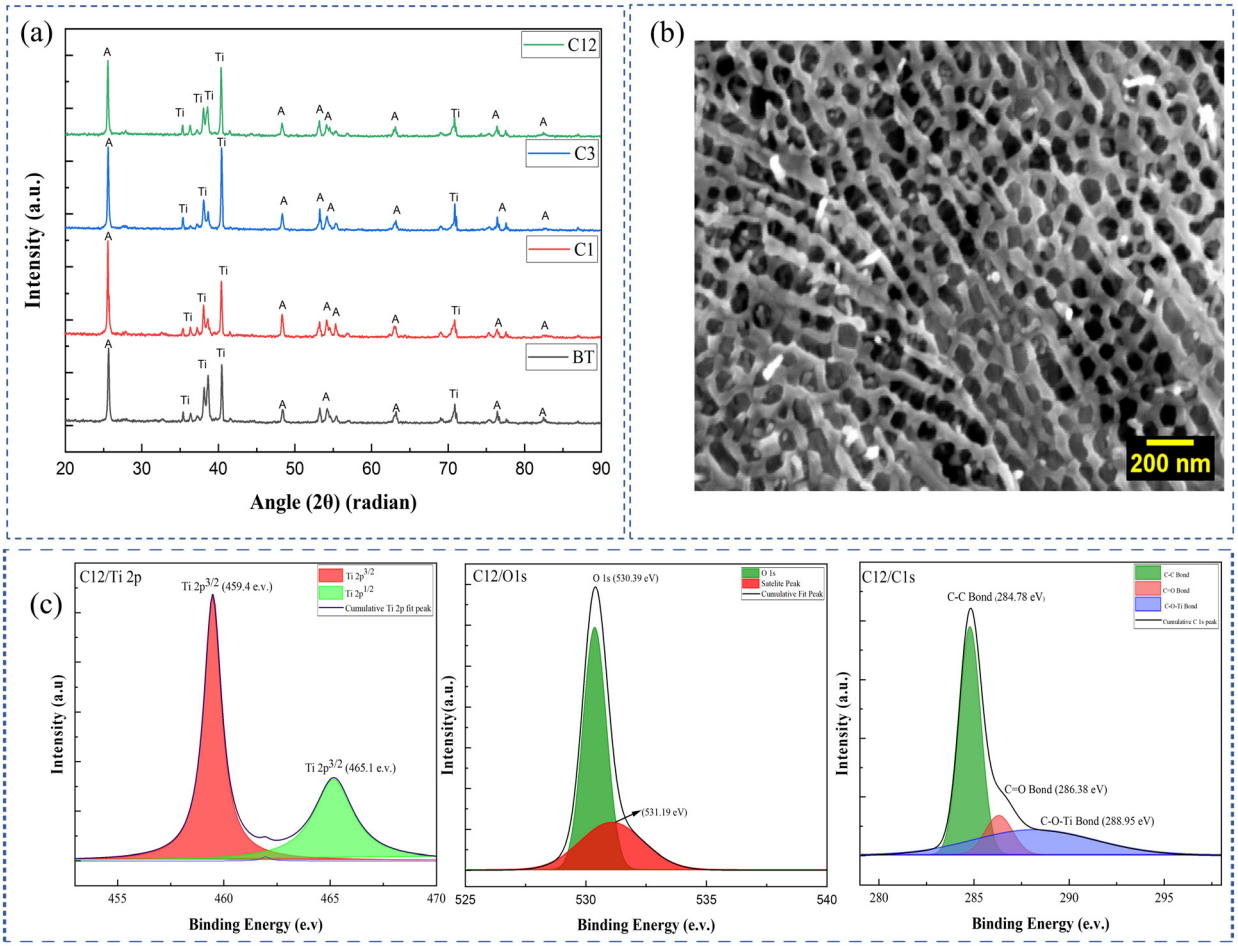

Fig. 9 (a) XRD patterns of the different samples after the stability test of BT, C1, C3 and C12, (b) FESEM of the top surface of C12 after the stability test and (c) XPS of C12 after the stability test.

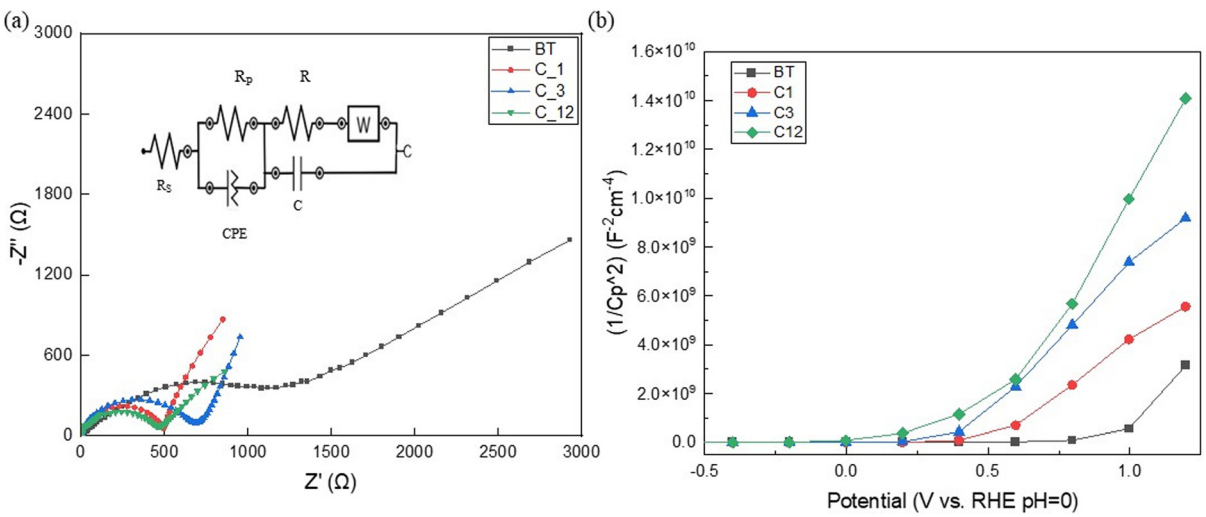

Fig. 10 (a) Nyquist plot and equivalent circuit of BT, C1, C3 and C12. (b) MS plot of B 40, C1, C3 and C12 recorded at a frequency of 1000 Hz.

of the active electrode system (R_S), the charge transfer resistance at the counter/electrolyte interface (R_P), which was parallel to the double-layer charge capacitance (CPE), and the bulk faradaic pseudo capacitance (C), which was parallel to the electrode–electrolyte interface (R) and the Warburg impedance (W), which corresponded to ion diffusion, in response to the impedance of the electrode. The fitting data are summarized in Table S2. According to the findings in Fig. 10(a), the charge transfer resistance (R_S) and the electrode material resistance (R) showed a remarkable lowering trend from 3.91 Ω, 3.65 Ω, 2.42 Ω to 1.05 Ω for the samples BT, C1, C3, and C12, respectively, suggesting that a significantly reduced resistance was incredibly beneficial for enhancing the electrochemical performance.

The Mott–Schottky analysis was widely used to determine the existence of defects on surface states at the electrode–electrolyte interface. As depicted in Fig. 10(b), the nanotube electrodes showed a positive slope corresponding to the n-type semiconductor behavior. The Mott–Schottky plot slopes for the electrodes of the carbon-doped sample and the bare TiO_2 were used to calculate the carrier densities (with the dielectric constant of TiO_2 being around 31). The carrier densities of the electrodes called BT, C1, C3, and C12 were 2.08×10^{18} cm^{-3}, 2.7×10^{18} cm^{-3}, 3.14×10^{19} cm^{-3} and 4.98×10^{19} cm^{-3}, respectively. Carbon-doped samples displayed ultra-high carrier densities due to a higher proportion of oxygen vacancies in TiO_2. Carbon-doped nanotube electrodes exhibited increased capacitance due to their improved conductivity and carrier density.

4. Conclusion

In conclusion, using the anodization method to improve the electrochemical capacitance in TiO_2 nanotube arrays, we have optimized the fabrication conditions by doping carbon in bare TiO_2. C-doped TiO_2 nanotubes have been found to have significantly increased charge-storage capabilities as supercapacitor electrode materials. The Raman and XPS analyses showed the successful doping of carbon in the titania nanotube arrays. Among the electrodes, the nanotube electrode fabricated by soaking in a carbon precursor for 12 hours showed an ultra-high carrier density of 4.98×10^{19} cm^{-3} and an areal capacitance of 8.125 mF cm^{-2} at 0.1 mA cm^{-2}. The impact of carrier concentration on the electrodes' charge transfer resistance was inferred by fitting the experimental data of the impedance spectra to an equivalent circuit model. The observed significant improvement was presumably due to the increased conductivity achieved by adding carbon species by subsequent dipping of the as-prepared samples by an anodization technique in the carbon precursors before giving thermal treatment. High-performance anodic metal oxides in domains connected to energy or the environment may be made possible by the simple method described in this paper.

Conflicts of interest

There are no conflicts to declare.

Data availability

Data will be made available on request.

Supplementary information (SI) is available. See DOI: https://doi.org/10.1039/d5nr04311e.

Acknowledgements

We acknowledge the funding from the South Asia Federation (SAF), the University Grants Commission (UGC). We acknowledge Central Instrumentation Facility (CIF) Pondicherry University for Characterization Facilities. We also acknowledge the HRTEM Facility at Centre for Nanoscience and Nanotechnology (CNSNT), Sathyabhama University and SCIF, SRMIST for XRD and HRSEM facilities. The authors are thankful to Pondicherry University for financial support. Soumya Jha would like to thank Dr. Aparna Markose, Department of Green Energy Technology, Pondicherry University for fruitful discussion.

References

1 Y. He, *et al.*, An overview of carbon materials for flexible electrochemical capacitors, *Nanoscale*, 2013, **5**, 8799.
2 V. Thirumal, R. Yuvakkumar, P. Senthil Kumar, G. Ravi and D. Velauthapillai, Direct growth of multilayered graphene nanofibers by chemical vapour deposition and their binder-free electrodes for symmetric supercapacitor devices, *Prog. Org. Coat.*, 2021, **161**, 106511.
3 S. Sandhiya and P. Elumalai, Enhanced active sites using LDH nanosheets@rGO as bifunctional cathode catalyst for high-capacity rechargeable Li-O2 battery, *Surf. Interfaces*, 2025, **60**, 106068–106080.
4 M. J. Carmezim and C. F. Santos, Electrolytes in Metal Oxide Supercapacitors, in *Metal Oxides in Supercapacitors*, Elsevier, 2017, pp. 49–78. DOI: 10.1016/b978-0-12-810464-4.00003-6.
5 Y. He, *et al.*, An overview of carbon materials for flexible electrochemical capacitors, *Nanoscale*, 2013, **5**, 8799.
6 M. Li, J. Lu, Z. Chen and K. Amine, 30 Years of Lithium–Ion Batteries, *Adv. Mater.*, 2018, **30**, 1800561.
7 C. C. Raj and R. Prasanth, Review—Advent of TiO 2 Nanotubes as Supercapacitor Electrode, *J. Electrochem. Soc.*, 2018, **165**, E345–E358.
8 Y.-Z. Zhang, *et al.*, Flexible supercapacitors based on paper substrates: a new paradigm for low-cost energy storage, *Chem. Soc. Rev.*, 2015, **44**, 5181–5199.
9 J. Wu, Understanding the Electric Double-Layer Structure, Capacitance, and Charging Dynamics, *Chem. Rev.*, 2022,

122, 10821–10859, DOI: 10.1021/acs.chemrev.2c00097. Preprint at DOI.

10 L. Zheng, *et al.*, Self-ordered Nanotubular TiO2 Multilayers for High-Performance Photocatalysts and Supercapacitors, *Electrochim. Acta*, 2016, **203**, 257–264.

11 K. V. G. Raghavendra, *et al.*, An intuitive review of supercapacitors with recent progress and novel device applications, *J. Energy Storage*, 2020, **31**, 101652.

12 C. Shi, L. Yan, Z. Wu, M. Lu and Z. Li, Ultrathin Ni(OH)2 nanosheets: Microemulsion assisted hydrothermal synthesis and application in advanced hybrid supercapacitors, *Surf. Interfaces*, 2024, **55**, 105472.

13 A. Markose, D. Das and P. Ravindran, Quantitative framework development for understanding the relationship between doping and photoelectrochemical energy conversion of TiO2, *Mater. Adv.*, 2023, **4**, 3399–3451, DOI: 10.1039/d3ma00059a. Preprint at DOI.

14 M. Isacfranklin, *et al.*, Hydrogen free direct growth carbon nanorod as a promising electrode in symmetric supercapacitor applications, *Prog. Org. Coat.*, 2021, **158**, 106379.

15 M. Goyal, K. Singh and N. Bhatnagar, Conductive polymers: A multipurpose material for protecting coating, *Prog. Org. Coat.*, 2024, **187**, 108083.

16 F. Mashkoor, *et al.*, Synergistic effect of heterointerface engineering coupled with oxygen vacancies enriched Ag2O-WO2.8-SnO2 anchored carbon nanotubes nanocomposite for high-performance supercapacitor devices and their charge storage mechanism, *Surf. Interfaces*, 2025, **62**, 106198.

17 J. Singh, *et al.*, Preparation of nickel oxide nanoparticles/biomass-derived activated carbon composites for high-performance aqueous asymmetric supercapacitor electrode, *Surf. Interfaces*, 2025, **56**, 105736.

18 X. Wang, Y. Liao and M. Johnson, Synthesis of Carbon-doped TiO2Nanotube Arrays and Their Application for Photocatalysis, in *IOP Conference Series: Earth and Environmental Science*, IOP Publishing Ltd, 2021, vol. 714.

19 A. Seetharaman, *et al.*, TiO2/Carbon allotrope nanohybrids for supercapacitor application with theoretical insights from density functional theory, *Appl. Surf. Sci.*, 2021, **563**, 150259.

20 K. Hemalatha, A. S. Prakash, K. Guruprakash and M. Jayakumar, TiO2 coated carbon nanotubes for electrochemical energy storage, *J. Mater. Chem. A*, 2014, **2**, 1757–1766.

21 C. Arumugam, *et al.*, Facile modification of TiO2 as S-Scheme multifunctional materials for environmental protection and energy-storage applications, *Surf. Interfaces*, 2024, **55**, 105298.

22 P. J. Morankar, R. U. Amate, A. M. Teli, S. A. Beknalkar and C.-W. Jeon, Synergistic effects of niobium phosphate/tungsten oxide core-shell nanocomposites for asymmetric supercapacitor, *Surf. Interfaces*, 2025, **56**, 105639.

23 M. Mohsen Momeni, H. Mohammadzadeh Aydisheh and B. K. Lee, Effectiveness of MnO_2 and V2O5 deposition on light fostered supercapacitor performance of WTiO2 nanotube: Novel electrodes for photo-assisted supercapacitors, *Chem. Eng. J.*, 2022, **450**, 137941.

24 J. Zhang, *et al.*, Remarkable supercapacitive performance of TiO2 nanotube arrays by introduction of oxygen vacancies, *Chem. Eng. J.*, 2017, **313**, 1071–1081.

25 L. Gao, D. Huang, Y. Shen and M. Wang, Rutile-TiO_2 decorated Li_4 Ti_5 O_{12} nanosheet arrays with 3D interconnected architecture as anodes for high performance hybrid supercapacitors, *J. Mater. Chem. A*, 2015, **3**, 23570–23576.

26 C. C. Raj, V. Srimurugan, A. Flamina and R. Prasanth, Tuning the carrier density of TiO2 nanotube arrays by controlling the oxygen vacancies for improved areal capacitance in supercapacitor applications, *Mater. Chem. Phys.*, 2020, **248**, 122925.

27 L. Wang, *et al.*, Nanoengineering S-Doped TiO_2 Embedded Carbon Nanosheets for Pseudocapacitance-Enhanced Li-Ion Capacitors, *ACS Appl. Energy Mater.*, 2018, **1**, 1708–1715.

28 M. M. Momeni and I. Ahadzadeh, Fabrication of tungsten decorated titania nanotube arrays as electrode materials for supercapacitor applications, *Int. J. Hydrogen Energy*, 2015, **40**, 8769–8777.

29 M. Najafi, M. Mohsen Momeni and B. K. Lee, Photo-rechargeable asymmetric supercapacitors based on nickel–cobalt sulfide on titania as novel photo-active electrodes, *Chem. Eng. J.*, 2024, **493**, 152423.

30 M. M. Momeni, H. M. Aydisheh, B. K. Lee, H. Farrokhpour and M. Najafi, Preparation of photo-rechargeable asymmetric supercapacitors using S,W-codoped titania: Experimental and theoretical insights, *J. Alloys Compd.*, 2023, **960**, 170722.

31 J. Zhang, *et al.*, Remarkable supercapacitive performance of TiO2 nanotube arrays by introduction of oxygen vacancies, *Chem. Eng. J.*, 2017, **313**, 1071–1081.

32 N. Li, *et al.*, Morphology construction and component tailoring of CoxNi1-xMoO4 solid solution nanotubes for high-performance hybrid supercapacitors, *Surf. Interfaces*, 2024, **51**, 104785.

33 Y. Tian, *et al.*, Fabrication of anatase TiO2/amorphous carbon nanoparticles as anode materials for enhanced lithium ion storage, *J. Phys. Chem. Solids*, 2020, **143**, 109524.

34 R. P. Vitiello, *et al.*, N-Doping of anodic TiO2 nanotubes using heat treatment in ammonia, *Electrochem. Commun.*, 2006, **8**, 544–548.

35 R. M. Tamgadge and A. Shukla, Fluorine-doped anatase for improved supercapacitor electrode, *Electrochim. Acta*, 2018, **289**, 342–353.

36 Q. Liu, *et al.*, A general approach to the fabrication of Sn-doped TiO2 nanotube arrays with titanium vacancies for supercapacitors, *Appl. Surf. Sci.*, 2021, **570**, 151175.

37 R. Kumar, *et al.*, In situ carbon-supported titanium dioxide (ICS-TiO2) as an electrode material for high performance supercapacitors, *Nanoscale Adv.*, 2020, **2**, 2376–2386.

38 J. H. Park, S. Kim and A. J. Bard, Novel carbon-doped TiO2 nanotube arrays with high aspect ratios for efficient solar water splitting, *Nano Lett.*, 2006, **6**, 24–28.
39 L. Zheng, *et al.*, High-performance supercapacitors based on amorphous C-modified anodic TiO2 nanotubes, *Appl. Surf. Sci.*, 2016, **362**, 399–405.
40 A. Rabbani, S. Jamshidi and S. Salehi, An automated simple algorithm for realistic pore network extraction from micro-tomography images, *J. Pet. Sci. Eng.*, 2014, **123**, 164–171.
41 A. Rabbani and S. Salehi, Dynamic modeling of the formation damage and mud cake deposition using filtration theories coupled with SEM image processing, *J. Nat. Gas Sci. Eng.*, 2017, **42**, 157–168.
42 G. M. K. Tolba, *et al.*, Synthesis of Novel Fe-Doped Amorphous TiO2 /C Nanofibers for Supercapacitors Applications, *Int. J. Electrochem. Sci.*, 2015, **10**, 3117–3123, https://www.electrochemsci.org.
43 A. Markose and P. Ravindran, Enhanced green hydrogen production via CdS/Cu-doped TiO2 nanotubes: Advancements in photoanode performance, *Electrochim. Acta*, 2024, **499**, 144704.
44 C. C. Raj, R. Sundheep and R. Prasanth, Enhancement of electrochemical capacitance by tailoring the geometry of TiO2 nanotube electrodes, *Electrochim. Acta*, 2015, **176**, 1214–1220.
45 C. Kim, S. Kim, J. Lee, J. Kim and J. Yoon, Capacitive and Oxidant Generating Properties of Black-Colored TiO_2 Nanotube Array Fabricated by Electrochemical Self-Doping, *ACS Appl. Mater. Interfaces*, 2015, **7**, 7486–7491.
46 H. Zhou, *et al.*, Three-dimensional nanoporous TiO2 network films with excellent electrochemical capacitance performance, *J. Alloys Compd.*, 2014, **597**, 1–7.
47 X. Lu, *et al.*, Hydrogenated TiO_2 Nanotube Arrays for Supercapacitors, *Nano Lett.*, 2012, **12**, 1690–1696.
48 G. D. Moon, J. B. Joo, M. Dahl, H. Jung and Y. Yin, Nitridation and layered assembly of hollow TiO2 shells for electrochemical energy storage, *Adv. Funct. Mater.*, 2014, **24**, 848–856.
49 M. H. Tong, *et al.*, Ultra-thin carbon doped TiO2 nanotube arrays for enhanced visible-light photoelectrochemical water splitting, *Appl. Surf. Sci.*, 2023, **623**, 156980.
50 M. Sipahi, *et al.*, Electrochemical impedance study of polyaniline electrocoated porous carbon foam, *Prog. Org. Coat.*, 2008, **62**, 96–104.
51 M. Ates, Review study of electrochemical impedance spectroscopy and equivalent electrical circuits of conducting polymers on carbon surfaces, *Prog. Org. Coat.*, 2011, **71**, 1–10.